ARTICLE

Self-assembled nanoparticles based on cationic mono-/AIE tetra-nuclear Ir(III) complexes: long wavelength absorption/near-infrared emission photosensitizers for photodynamic therapy

Received 00th January 20xx,
Accepted 00th January 20xx

DOI: 10.1039/x0xx00000x

Ziwei Wang,[‡a] Lijuan Li,[‡a] Weijin Wang,[a] Runlin Wang,[a] Guangzhe Li,[*c] Hang Bian,[*b] Dongxia Zhu[*a] and Martin R. Bryce[*d]

Cyclometalated Ir(III) complexes as photosensitizers (PSs) have attracted widespread attention because of their good photostability and efficient $^1O_2$ production ability. However, their strong absorption in the UV-vis region severely limits their applications in photodynamic therapy (PDT) because the short wavelength illuminating light can be easily absorbed by the skin and subcutaneous adipose tissue causing damage to the patient's normal tissue. Herein, mono- and tetra-nuclear Ir(III) complex-porphyrin conjugates are rationally designed and synthesized, especially **[TPP-4Ir]$^{4+}$** exhibits obvious aggregation-induced emission (AIE) characteristics. PSs comprising Ir(III) complex-porphyrin conjugates self-assembled as nanoparticles (NPs) are successfully achieved. The obtained **[TPP-Ir]$^{+}$** NPs and **[TPP-4Ir]$^{4+}$** NPs exhibit long wavelength absorption (540-700 nm) and near-infrared emission (635-750 nm), successfully overcoming the inherent defects of short wavelength absorption of traditional Ir(III) complexes. Moreover, **[TPP-4Ir]$^{4+}$** NPs exhibit good biocompatibility, high $^1O_2$ generation ability, low half-maximal inhibitory concentration (IC_{50}) (0.47×10^{-6} M), potent cytotoxicity toward cancer cells and superior cellular uptake under white light irradiation. This work extends the scope for transition metal complex PSs with promising clinical applications.

Introduction

Photodynamic therapy (PDT) is a typical non-invasive treatment which has been widely used in the treatment of lung cancer, skin cancer, esophageal cancer and so on.[1-3] The process of PDT depends on the effective combination of non-toxic photosensitizers (PSs), oxygen and a light source. Under light irradiation, a PS converts oxygen into cytotoxic reactive oxygen species (ROS), which triggers biological reactions within a patient and eventually leads to cell death.[4] The ideal PSs should have strong absorption in the phototherapy window (600-900 nm) to ensure the full efficacy of PDT in deep tissue, significant singlet-to-triplet excited state intersystem crossing (ISC) ability to promote the production of ROS, and good biocompatibility.[5-7]

Cyclometalated Ir(III) complexes as PSs have attracted wide attention because of their good photostability, versatility for ligand modification, heavy-atom induced strong spin-orbit coupling and intersystem crossing (ISC) capacity, and efficient $^1O_2$ production ability. For examples, Martinez-Alonso et al reported the strong influence of the ancillary ligand over the PDT properties of neutral bis(cyclometallated) Ir(III) complexes.[8a] Chao's group reported that an iridium complex-based magnetothermal nanoenzyme (Ir@$MnFe_2O_4$NPs) that targets mitochondria can be used for efficient cancer

[a] *Key Laboratory of Nanobiosensing and Nanobioanalysis at Universities of Jilin Province, Department of Chemistry, Northeast Normal University, 5268 Renmin Street, Changchun, Jilin Province 130024, P. R. China.*
E-mail: zhudx047@nenu.edu.cn
[b] *School of Material Science and Engineering, Jilin Jianzhu University, Changchun 130118, China.*
Email: bhspring@gmail.com
[c] *Jilin Provincial Science and Technology Innovation Center of Health Food of Chinese Medicine, Changchun University of Chinese Medicine, Changchun, Jilin Province 130117, P. R. China.*
E-mail: 1993008106@qq.com
[d] *Department of Chemistry, Durham University, Durham, DH1 3LE, UK.*
E-mail: m.r.bryce@durham.ac.uk
† Electronic Supplementary Information (ESI) available: Supporting Figures and Tables. See DOI: 10.1039/x0xx00000x
‡ The authors contributed equally to the preparation of this work.

treatment.[8b] Zhao et al developed a functionalized iridium complex with a long-lived intraligand triplet excited state as a PS for PDT under hypoxic conditions, representing a significant advance for PDT.[9] Although cyclometalated Ir(III) complexes have these advantages, their longest wavelength absorption band is typically quite weak and is usually located in the UV-vis region. Short wavelength light is readily absorbed by the skin and subcutaneous adipose tissue causing damage to a patient's normal tissue, thereby limiting the clinical application of iridium complex PSs in PDT.[10, 11] In order to mitigate this problem, ligands with extended π–conjugation have been successfully employed.[12] Alternative strategies include two-photon excitation (TPE) [13, 14] and the introduction of upconversion nanoparticles (UCNPs). [15] However, these methods still possess some shortcomings, such as complex equipment, low conversion efficiency, high cost and potential biotoxicity, which will bring new challenges to clinical applications. [16, 17] At same time, cyclometalated Ir(III) complexes PSs still suffer from the drawback of traditional PSs : aggregation-caused quenching (ACQ). Tang and co-workers promoted the aggregation-induced emission (AIE) phenomenon in 2001,[18] by which intramolecular motion is restricted in an aggregate state to prohibit the dissipation of energy.[19] PSs with AIE characteristics have shown improved ROS generation upon aggregation and displayed great potential for enhanced PDT effects.[20] Therefore, how to choose an appropriate molecular design strategy to construct AIE cyclometalated Ir(III) complexes PSs with optimal absorption capacity is important to further improve their performance and realize their clinical application in PDT.

Porphyrin is one of the ideal therapeutic drugs. [21] Thanks to its unique spectral characteristics, especially the absorption in the red/near-infrared (NIR) region, its application as PSs in PDT has attracted wide attention. Zhang's group engineered a porphyrin-containing Covalent Organic Polymer (COP) framework to realize highly specific PDT to overcome the drug resistance of hypoxic tumors.[22] Zhang and colleagues reported a porphyrin/POSS alternating copolymer to enhance PDT efficacy (POSS = polyhedral oligomeric silsesquioxane).[23] It is well known that cyclometalated Ir(III) complexes have a typical octahedral configuration and are easily functionalized through adjusting their ligands. [24, 25] It is expected that porphyrin molecules with long wavelength absorption could be covalently linked to the auxiliary ligands of Ir(III) complexes through a reasonable design strategy. In our previous work, we found that the multinuclear neutral Ir(III) complexes show stronger ability to produce $^1O_2$ due to the increase of metallic iridium centers compared with a mononuclear analogy; nevertheless their synthesis and purification processes were complicated and had low overall yields.[26]

Nanoparticles (NPs) which are constructed with negligible dark toxicity and good water solubility by introducing an amphiphilic polymer or nanocarriers, suffer from the drawback of expensive cost, sophisticated synthetic protocols and complicated structural modifications owing to the presence of multiple components. These negative factors are barriers for large-scale production and practical clinical applications of NPs. [27-29] Therefore, increased attention has been paid to the self-assembly of carrier-free nanoparticles by electrostatic interactions, hydrophobic effects or π-conjugated structures of organic molecules.[30,31] But so far, only a few Ir(III) complex-based NPs obtained by self-assembly methods have been reported. There remains, therefore, considerable scope to achieve good biocompatibility for cell imaging and PDT using transition metal complex PSs.[32]

Based on above considerations, we considered that PSs comprising self-assembled NPs of cationic porphyrin-multinuclear Ir(III) complexes might be a feasible design strategy to achieve the high performance of transition metal complexes in PDT. In this work, a tetraphenylporphyrin (TPP) unit is incorporated into mono-/AIE tetra-Ir complexes by simple high-yielding Schiff base reactions. The $(C^N)_2(N^N)$ ligands result in a cationic structure of the Ir complexes which was designed to enhance lipophilicity, cellular uptake and internalization of the PSs, as reported for other cationic transition metal complexes.[33] The obtained mononuclear and tetranuclear cationic iridium complexes (**[TPP-Ir]**$^+$and **[TPP-4Ir]**$^{4+}$) exhibit long wavelength absorption and near infrared emission, successfully overcoming the inherent defects of short wavelength absorption of traditional iridium complexes.

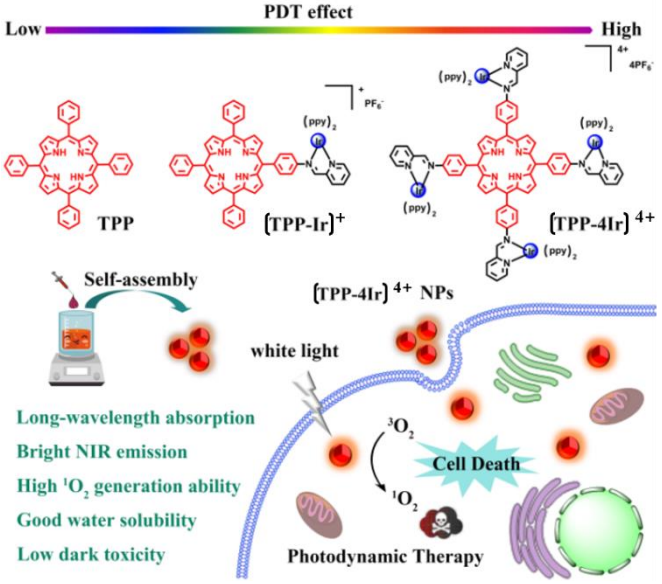

Scheme 1 Chemical structures of **TPP**, **[TPP-Ir]**$^+$ and **[TPP-4Ir]**$^{4+}$ and design principle of **[TPP-4Ir]**$^{4+}$ as PS for PDT.

Without any auxiliary reagents, the corresponding carrier-free NPs, namely **[TPP-Ir]**$^+$ NPs and **[TPP-4Ir]**$^{4+}$ NPs, were successfully obtained by straightforward self-assembly methods. The results of spectroscopic and cell experiments show that the tetranuclear **[TPP-4Ir]**$^{4+}$ NPs present strong long-wavelength

absorption and bright near-infrared emission. Excellent ability to produce $^1O_2$, negligible dark toxicity and outstanding phototoxicity are achieved with **[TPP-4Ir]$^{4+}$** NPs under white light activation. The introduction of multiple metal centers and extended π–conjugation significantly improve the ability to generate $^1O_2$, thus enhancing the PDT effect compared to the mono-Ir analogy. **TPP** NPs were studied as a model system. This work provides a new avenue for developing the clinical applications of Ir(III) complex PSs in PDT (Scheme 1).

Experimental section

Materials and instruments

Materials for organic synthesis, poloxamer (F127) and indocyanine green (ICG) were purchased from Energy Chemical Company. RPMI Medium 1640 was purchased from Solarbio Life Science company. Fetal bovine serum (FBS) was purchased from Sigma-Aldrich. 3-(4, 5-Dimethylthiazol-2-yl)-2,5-diphenyltetrazolium bromide (MTT) was obtained from Aladdin. 2',7'-Dichlorofluorescence diacetate (DCFH-DA) and the cell viability (live/dead cell staining) assay kit were purchased from Shanghai Beyotime Biotechnology Co. Ltd.

^{1}H NMR spectra were recorded at 25 °C on a Varian 600 MHz spectrometer. The high resolution mass spectra (HRMS) were obtained on a high-performance liquid chromatography-high-resolution time of flight mass spectrometer (MicroTOF II). UV-vis absorption spectra were recorded on a Shimadzu UV-3100 spectrophotometer. The photoluminescence spectra, excited state lifetimes (τ) and photoluminescence quantum yields (Φ_{PL}) were recorded on an Edinburgh FLS920 spectrofluorimeter under air at room temperature. Transmission electron microscopy (TEM) images were taken by a TECNAI F20 microscope. Diameter and diameter distribution of the nanoparticles were determined by a Malvern Zetasizer Nano instrument for dynamic light scattering (DLS).

Preparation of nanoparticles (NPs)

The water-soluble NPs were prepared by the solvent exchange method. **TPP**, **[TPP-Ir]$^+$** or **[TPP-4Ir]$^{4+}$** (2 mg) was dissolved in acetone (2 mL), and surfactant F127 in THF (2 mL). The mixture was then added dropwise into deionized water (10 mL) with stirring at a uniform speed. After the acetone / THF had completely evaporated, the solution was collected and dialyzed. Finally, the dialysate was filtered with a 0.45 μm filter to obtain uniformly dispersed nanoparticles. The concentration of NPs can be calculated by the corresponding standard curve.[34-36] The hydrodynamic sizes and morphologies of the NPs were analyzed by dynamic light scattering (DLS) and transmission electron microscopy (TEM).

Singlet oxygen generation

The $^1O_2$ production ability of **TPP** NPs/**[TPP-Ir]$^+$** NPs/**[TPP-4Ir]$^{4+}$** NPs was evaluated using 9,10-anthracenyl-bis(methylene)malonic acid (ABDA) as the capture agent, and the UV-visible absorption spectrum was used to monitor the change of ABDA's absorption intensity at 378 nm. Briefly, the mixture of ABDA (1 mg mL^{-1}, 70 μL) and **TPP** NP$_S$ or **[TPP-Ir]$^+$** NPs or **[TPP-4Ir]$^{4+}$** NPs (5×10^{-6} M) was transferred to a cuvette, and then illuminated them under a white LED at 20 mW cm^{-2} for 20 s. The generation of $^1O_2$ was determined according to the absorbance that decreased with time.

Cell culture and cytotoxicity

The cytotoxicity of the PSs was evaluated by MTT assay. Firstly, HeLa cells were seeded in a 6-well plate at a density of about 10,000 cells per well and incubated overnight. Then media containing different concentrations of PS (0-4 μM) were added to the wells, respectively. After 6 hours, the light group was irradiated with a white LED lamp for 25 minutes, while the dark group was not irradiated. After 24 hours, MTT (20 μL, 5 mg mL^{-1}) was added to culture the cells for 4 hours.

Live/dead cell staining

HeLa cells were seeded in 96-well plates at around 10,000 cells per well and incubated overnight. Medium containing PS (4 μM) was then added to the wells separately. After 6 hours, the light group was irradiated with a white LED lamp at 20 mW cm^{-2} for 25 min, while the dark group was not irradiated; then, all the cells were cultured for an additional 24 h. Finally, the cells were imaged by a fluorescence microscope after treatment with Calcein-AM and propidium iodide (PI) solutions.

Cell uptake

Confocal laser scanning microscopy (CLSM) images were taken using a ZeissLSM 700 (Zurich, Switzerland). HeLa cells were incubated overnight in a 6-well plate with a density of about 50,000 cells per well. Medium containing PS (4 μ M) was incubated for 0.5 h, 2 h and 6 h, respectively, then fixed with 4% paraformaldehyde (1 mL) for 10 min. Hoechst 33258 was used as a nuclear dye, then sliced and packaged. Finally, the slides were observed by CLSM with excitation at 488 nm.

Results and discussion

Synthesis and characterization

The chemical structures of complexes **TPP**, **[TPP-Ir]$^+$** and **[TPP-4Ir]$^{4+}$** are shown in Scheme 1. The synthesis routes to **L1** and **L4**, **[TPP-Ir]$^+$** and **[TPP-4Ir]$^{4+}$** (Scheme S1-S4) and corresponding characterization are provided in the Electronic Supplementary Information (ESI) with ^{13}C{^{1}H} NMR spectra and mass spectra (Fig. S1-8). The self-assembled **TPP** NPs, **[TPP-Ir]$^+$** NPs and **[TPP-4Ir]$^{4+}$** NPs were prepared by diluting acetonitrile (ACN) solutions of **TPP**, **[TPP-Ir]$^+$** and **[TPP-4Ir]$^{4+}$** with aqueous media.

The size and morphology of NPs have great influence on their subsequent biomedical applications. The micro-morphology and size of the NPs were determined by dynamic light scattering (DLS) and transmission electron microscopy (TEM) respectively. Fig. 1 shows that the average hydrodynamic diameters of **TPP** NPs, **[TPP-Ir]**$^{+}$ NPs and **[TPP-4Ir]**$^{4+}$ NPs are 155 nm, 115 nm and 135 nm, respectively. **TPP** NPs, **[TPP-Ir]**$^{+}$ NPs and **[TPP-4Ir]**$^{4+}$ NPs all have uniform spherical shape and the average size is 133 nm, 100 nm and 116 nm, respectively, by TEM (Fig. 1 inset). Compared with the size measured by DLS, the larger size measured by TEM can be attributed to a hydrated layer on the NPs.[37] Moreover, the size or size distribution of the **TPP** NPs, **[TPP-Ir]**$^{+}$ NPs and **[TPP-4Ir]**$^{4+}$ NPs show no obvious changes within seven days, which indicates that these NPs with spherical morphology and appropriate size have good stability. These properties are conducive to their subsequent application in cells.

Photophysical properties

The photophysical properties of **TPP** NPs, **[TPP-Ir]**$^{+}$NPs and **[TPP-4Ir]**$^{4+}$ NPs in pure water were investigated by UV-vis absorption and photoluminescence (PL) spectroscopy. As shown in Fig. 2, the relatively strong absorption bands of **[TPP-Ir]**$^{+}$ NPs and **[TPP-4Ir]**$^{4+}$ NPs in the range of 250 - 350 nm originate from the π-π* transition of the ligand center, and at 350- 500 nm partly from a combination of metal-to-ligand charge transfer (^{1}MLCT), ligand-to-ligand charge transfer (^{1}LLCT), spin-forbidden metal-to-ligand charge-transfer (^{3}MLCT) and spin-forbidden ligand-to-ligand charge-transfer (^{3}LLCT).[25] The characteristic absorption bands in the 500-700 nm range derive from the porphyrin moiety, indicating that the iridium complexes with long wavelength absorption are successfully constructed by the combination with a porphyrin unit.[38]

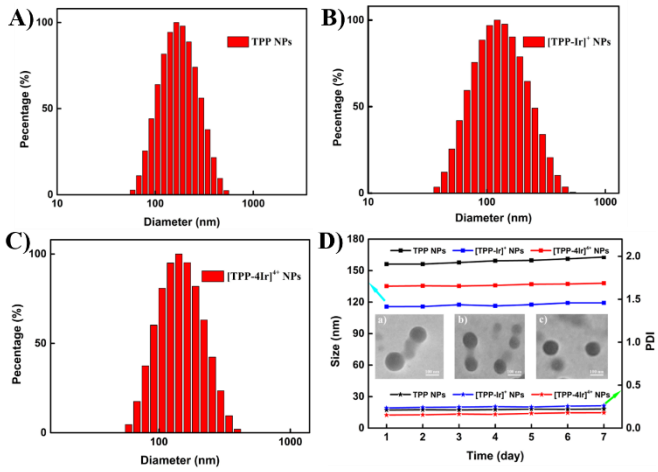

Fig. 1 DLS diagram of A) **TPP** NPs, B) **[TPP-Ir]**$^{+}$ NPs and C) **[TPP-4Ir]**$^{4+}$ NPs; D) Size and PDI changes of NPs within a week; the insets are TEM images of NPs.

The UV-Vis absorption spectra of the corresponding pure compounds, **TPP**, **[TPP-Ir]**$^{+}$ **and [TPP-4Ir]**$^{4+}$, exhibit similar absorption bands in acetone (Fig. S9). The extended absorption bands of **[TPP-Ir]**$^{+}$ **and [TPP-4Ir]**$^{4+}$ in the 500–700 nm region are advantageous for matching long-wavelength excitation to enhance tissue penetration. As in our previous work,[26] it is worth noting that the molar absorption coefficients corresponding to the maximum absorption wavelength have been obviously enhanced due to the introduction of the extra iridium centers and the extended π-conjugation of the porphyrin auxiliary ligands which are in the order: **[TPP-4Ir]**$^{4+}$ NPs > **[TPP-Ir]**$^{+}$ NPs > **TPP** NPs (Fig. 2A and Table S2). The molar absorption coefficient around 420 nm follows the sequence **[TPP-4Ir]**$^{4+}$ NPs (184870 M^{-1} cm^{-1}) > **[TPP-Ir]**$^{+}$ NPs(138510 M^{-1} cm^{-1}) > **TPP** NPs(115730 M^{-1} cm^{-1}). The molar absorption coefficients of **[TPP-4Ir]**$^{4+}$ NPs and **[TPP-Ir]**$^{+}$ NPs at 650 nm are 3.15 and 1.85 times higher than that of **TPP** NPs respectively. Long wavelength absorption with high molar absorption coefficients is advantageous for PSs to obtain the desired enhanced tissue penetration.[22a,39] These results indicate that the NPs are candidates to realize clinical PDT under white-light activation which can effectively avoid the patients suffering significant pain from UV-Vis light irradiation.[40]

As shown in Fig. S10, **[TPP-4Ir]**$^{4+}$ exhibited weak emission in pure acetone, but emits bright near-infrared phosphorescence when the water content gradually increases to 80%, which is a typical AIE characteristic. In contrast, **[TPP-Ir]**$^{+}$ showed obvious AIE phenomenon. In addition, it can be seen from the PL spectra (Fig. 2B) that **TPP** NPs, **[TPP-Ir]**$^{+}$ NPs and **[TPP-4Ir]**$^{4+}$ NPs all show a strong emission peak at about 656 nm in the red region and a weaker peak at about 720 nm in the near-infrared region. However, the PL intensities of the NPs significantly decreased in the order **TPP** NPs > **[TPP-Ir]**$^{+}$ NPs > **[TPP-4Ir]**$^{4+}$ NPs. The emission intensity of **TPP** NPs at 720 nm is 2.51 and 4.13 times higher than those of **[TPP-Ir]**$^{+}$ NPs and **[TPP-4Ir]**$^{4+}$, respectively. The photoluminescence quantum yields (PLQYs) and excited-state lifetimes of **TPP** NPs, **[TPP-Ir]**$^{+}$ NPs and **[TPP-4Ir]**$^{4+}$ NPs and their corresponding photophysical data are summarized in Table S1. The PLQYs of **TPP** NPs, **[TPP-Ir]**$^{+}$ NPs and **[TPP-4Ir]**$^{4+}$ NPs in water are 27.1%, 8.1%, and 3.6%, respectively. The excited-state lifetimes (τ) of **TPP** NPs, **[TPP-Ir]**$^{+}$ NPs and **[TPP-4Ir]**$^{4+}$ NPs in water are very similar at 5.47, 5.72, and 5.87 ns, respectively.

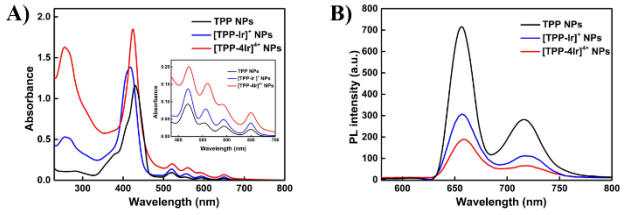

Fig. 2 A) UV-vis absorption spectra of **TPP** NPs, **[TPP-Ir]**$^{+}$ NPs and **[TPP-4Ir]**$^{4+}$ NPs in water(10^{-5} M); the inset is the enlarged absorption spectra from 540-700 nm. B) PL spectra of **TPP** NPs, **[TPP-Ir]**$^{+}$ NPs and **[TPP-4Ir]**$^{4+}$ NPs in water(10^{-5} M) under 365 nm UV irradiation.

The k_r values decrease sequentially from **TPP** NPs > **[TPP-Ir]**$^{+}$ NPs > **[TPP-4Ir]**$^{4+}$ NPs, while **[TPP-4Ir]**$^{4+}$ NPs show the highest k_{nr} in the series of NPs. These results indicate that the accelerated transfer of excited energy to the triplet state and to nonradiative vibrational processes could be realized to improve the efficiency of PDT due to

the increased molar absorbance coefficient and the reduced emission performance.[41] These data indicate that the fluorescence of **[TPP-Ir]**$^{+}$ NPs and **[TPP-4Ir]**$^{4+}$ NPs is from the porphyrin unit and the phosphorescent Ir complexes are not emitting. These results suggest that the full energy transfer between **[TPP-4Ir]**$^{4+}$ NPs and oxygen molecules in the PDT process could generate singlet oxygen with high efficiency. **[TPP-4Ir]**$^{4+}$ NPs with long wavelength absorption and near-infrared emission therefore hold great promise for highly efficient PDT under white light irradiation.

Evaluation of singlet oxygen generation capability in solution

PSs need to be activated by light to produce $^1O_2$, which will cause cancer cell tissue damage. Therefore, it is of great significance to study the production capacity of $^1O_2$ for the applications of PDT. Because the iridium complex-porphyrin conjugates have a wide absorption range (400-700 nm) we selected a white light LED lamp (400-700 nm, 20 mW cm^{-2}) as the irradiation source to evaluate the $^1O_2$ generation ability by using 9,10-anthracenediyl-bis(methylene)dimalonic acid (ABDA) as an indicator through monitoring the change in the absorbance of ABDA at 300-500 nm. As shown in Fig. S12-14, no obvious changes of absorbance were observed in three control groups: (1) ABDA and PSs without irradiation; (2) PSs with irradiation; (3) only ABDA with irradiation, suggesting that all the PSs show good photostability.[42] On the contrary, the absorption peak of ABDA at 790 nm gradually decreases in intensity upon irradiation of ABDA solutions in the presence of **TPP** NPs, **[TPP-Ir]**$^{+}$ NPs and **[TPP-4Ir]**$^{4+}$ NPs, verifying that the PSs possess excellent $^1O_2$ generation ability (Fig. 3A and Fig. S15). The decrease of ABDA absorption induced by **[TPP-Ir]**$^{+}$ NPs and **[TPP-4Ir]**$^{4+}$ NPs was much higher than that of **TPP** NPs, which indicated that the iridium centers facilitate the $^1O_2$ production. As shown in Fig. 3B and C, all the PSs follow a first-order $^1O_2$ generation behaviour. The slopes can be ordered as **TPP** NPs < **[TPP-Ir]**$^{+}$ NPs < **[TPP-4Ir]**$^{4+}$ NPs. The kinetic decays of **[TPP-4Ir]**$^{4+}$ NPs are 5.9 times and 55.5 times that of **[TPP-Ir]**$^{+}$ NPs and **TPP** NPs, respectively. A steeper slope represents a quicker decay rate of ABDA and increased ability to generate $^1O_2$. Overall, **[TPP-4Ir]**$^{4+}$ NPs generate $^1O_2$ very effectively and they have a high potential as PSs for clinical applications in the future.

Evaluation of intracellular singlet oxygen production capacity

2,7-Dichlorodihydrofluorescein diacetate (DCFH-DA) does not emit light and can be hydrolyzed by intracellular esterase and converted to 2,7-dichlorodihydrofluorescein (DCFH) when it enters cells. DCFH can generate the green fluorescent molecule 2,7-dichlorofluorescein (DCF) by reacting with $^1O_2$ - the greater the amount of $^1O_2$, the stronger the fluorescent signal generated.[43,44] As shown in Fig. 3D, negligible green fluorescence was observed by CLSM from Hela cells in the blank control group and from **[TPP-4Ir]**$^{4+}$ NPs without light irradiation, meaning an absence of $^1O_2$ generation in **[TPP-4Ir]**$^{4+}$ NPs. Conversely, bright green emission was observed from the cells in the **[TPP-4Ir]**$^{4+}$ NPs group in the presence of white light irradiation while the control group still showed no fluorescence, which suggests the excellent intracellular $^1O_2$ production of **[TPP-4Ir]**$^{4+}$NPs. These results indicated that **[TPP-4Ir]**$^{4+}$ NPs can be used as an effective PS in PDT.

Cytotoxicity test

As the tetra-nuclear **[TPP-4Ir]**$^{4+}$ NPs have good photophysical properties and high-efficiency intracellular $^1O_2$ production capacity, the cytotoxicity of **[TPP-4Ir]**$^{4+}$ NPs in HeLa cells was analyzed by a standard 3-(4,5-dimethylthiazol-2-yl)-2,5-diphenyltetrazolium bromide (MTT) assay. As shown in Fig. 4A, after **[TPP-4Ir]**$^{4+}$ NPs were incubated with HeLa cells for 24 h in the dark, the cell viability exceeded 95%, indicating that **[TPP-4Ir]**$^{4+}$ NPs had good cytocompatibility and negligible dark cytotoxicity. On the contrary, when white light irradiation (400-700 nm, 20 mW cm^{-2}) was used for 25 min, the viability of the HeLa cells decreased significantly with the increasing concentration of **[TPP-4Ir]**$^{4+}$ NPs, meaning that **[TPP-4Ir]**$^{4+}$ NPs showed a concentration-dependent cytotoxicity. It is worth noting that the maximum half inhibitory concentration (IC_{50}) of **[TPP-4Ir]**$^{4+}$ NPs is 0.47× 10^{-6} M, and such a low IC_{50} value indicates the potential PDT effect of **[TPP-4Ir]**$^{4+}$ NPs.

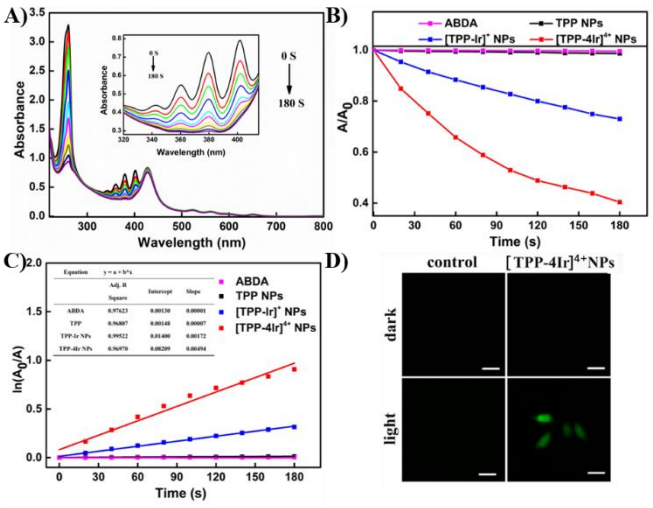

Fig. 3 A) **[TPP-4Ir]**$^{4+}$ NPs (5 × 10^{-6} M) UV-vis absorption spectra of ABDA irradiated by white light (400-700nm, 20 mW cm^{-2}). B) The decomposition rates of ABDA with different PSs by white light (400-700 nm, 20 mW cm^{-2}). C) Time-dependent kinetics of $^1O_2$ generation. A_0 = absorption of DPBF without irradiation. A = real-time absorption of ABDA with different irradiation times. D) Fluorescence image of intracellular $^1O_2$ produced by **[TPP-4Ir]**$^{4+}$ NPs after exposure to DCFH-DA for 10 min. Scale bar = 20 μm for all images.

Live/dead cell staining experimental study

In order to confirm the PDT effect of **[TPP-4Ir]**$^{4+}$ NPs more rigorously, the Calcein-AM and propidium iodide (PI) double fluorescence staining method was used. As shown in Fig. 4B, a large area of strong green fluorescence and a very weak red fluorescence signal were observed for the control group and **[TPP-4Ir]**$^{4+}$ NPs in the dark, suggesting a lower dark toxicity and good biocompatibility of **[TPP-**

4Ir]$^{4+}$ NPs. Under white light irradiation, negligible green fluorescence and strong red fluorescence signal were observed which indicates that the HeLa cells were effectively killed. All these results are consistent with the MTT experiment that **[TPP-4Ir]$^{4+}$** NPs have excellent phototoxicity and low dark toxicity.

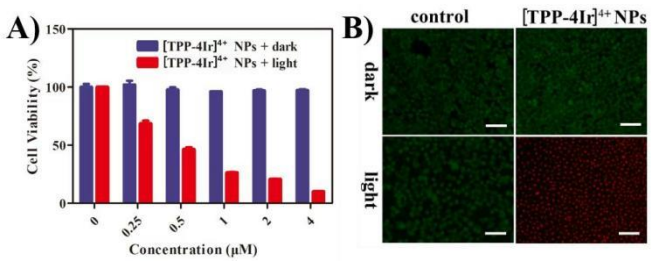

Fig. 4 A) Relative viability of HeLa cells after 24 h co-incubation with **[TPP-4Ir]$^{4+}$** NPs under darkness and under white light irradiation (20 mW cm^{-2}, 60 min); B) Confocal fluorescence images of HeLa cells co-stained with Calcein-AM (live cells, green fluorescence) and propidium iodide (dead cells, red fluorescence) after treatment with **[TPP-4Ir]$^{4+}$** NPs (10 μg mL^{-1}). Scale bar = 20 μm for all images.

Cell endocytosis test

After exploring the cytotoxicity of **[TPP-4Ir]$^{4+}$** NPs, we used CLSM to characterize the internalization effect of **[TPP-4Ir]$^{4+}$** NPs. The efficient uptake of PSs by cells is a premise for good PDT. As shown in Fig. 5, the fluorescence signal generated in the cells gradually increased with the extension of the culture time, indicating that the cellular uptake was time-dependent. Time-dependent near-infrared fluorescence signals in the cytoplasm can be observed. In addition, with the gradual extension of culture time from 0.5 h to 6 h, the enhanced near infrared fluorescence signal was observed, which proved that **[TPP-4Ir]$^{4+}$** NPs could be effectively internalized by HeLa cells.

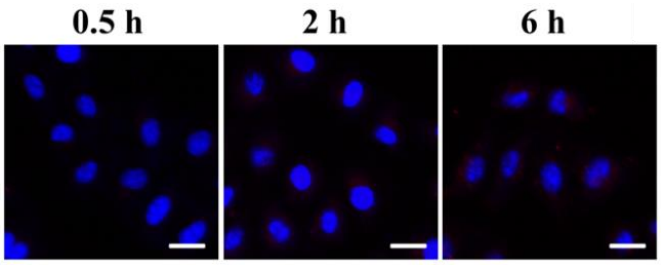

Fig. 5 CLSM images of **[TPP-4Ir]$^{4+}$** NPs incubated with HeLa cells for 0.5 h, 2 h and 6 h under the white light LED at 20 mW cm^{-2} for 15 min using DCFH-DA as an indicator. Scale bar =20 μm for all images.

Conclusions

In summary, we have rationally designed and synthesized new cationic mono- and AIE tetra-nuclear Ir(III) complex-porphyrin conjugates and obtained their corresponding carrier-free NP PSs, namely **[TPP-Ir]$^{+}$** NPs and **[TPP-4Ir]$^{4+}$** NPs, by self-assembly without any auxiliary reagents, for highly efficient PDT. This work combines the benefits of a porphyrin unit and cationic cyclometalated Ir(III) complexes to give PSs with long-wavelength absorption at 540-700 nm and near infrared emission (635-750 nm). This strategy has overcome the drawback of short wavelength absorption of traditional iridium complexes. In addition, the metal centers significantly increase the absorption capacity at long wavelength compared to pure tetraphenylporphyrin (**TPP**), resulting in the significantly enhanced generation of $^1O_2$. The new cationic molecules and their NPs have the following particular attributes: (i) straightforward, high yielding synthesis from readily available starting materials; (ii) carrier-free NPs were used successfully as PSs; (iii) white light photosensitization was efficiently achieved. Most importantly, the tetranuclear **[TPP-4Ir]$^{4+}$** NPs have strong long-wavelength absorption, bright near-infrared emission and high-efficiency $^1O_2$ generation capacity. Cell experiments show that **[TPP-4Ir]$^{4+}$** NPs exhibited good biocompatibility, negligible dark toxicity and excellent phototoxicity, demonstrating their potential for future clinical applications.

Conflicts of interest

There are no conflicts to declare.

Acknowledgements

This work was funded by NSFC (Grants No. 52073045，51903101), the Development and Reform Commission of Jilin Province (2020C035-5), and Changchun Science and Technology Bureau (CC202110378310002101). M. R. B. thanks EPSRC (UK) grant EP/L02621X/1 for funding. D. Zhu is grateful for the support from the Key Laboratory of Nanobiosensing and Nanobioanalysis at the Universities of Jilin Province. The authors acknowledge the support from Pro. Zhigang Xie and the Jilin Provincial Department of Education.

Notes and references

1 N. J. Sanfilippo, A. Hsi, A. S. DeNittis, G. G. Ginsberg, M. L. Kochman, J. S. Friedberg and S. M. Hahn, *Lasers Surg. Med.*, 2001, **28**,278-281.

2 P. Cai, W. Yang, Z. He, H. Jia, H. Wang, W. Zhao. L. Gao, Z. Zhang, F. Gao and X. Gao, *Biomater. Sci*., 2020, 8, 4841-4851.

3 F. Valli, M. C. G. Vior, L. P. Roguin and J. Marino, *Free. Radic. Biol. Med*., 2020, 152, 743-754.

4 S. Ding, Z. Liu, C. Huang, N. Zeng, W. Jiang and Q. LI, *ACS Appl. Mater. Interfaces*, 2021, 13, 10564-10573.

5 Y. Dong, G. Li, L. Wang, L. Cao, Y. Li and W. Zhao, *J. Photochem. Photobiol., B*, 2020, 211, 112015.

6 R. Guo, J. Yin, Y. Ma, Q.Wang and W. Lin, *J. Mater. Chem. B*, 2018, 6, 2894-2900.

7 R. Tian, W. Sun, M. Li, S. Long, M. Li, J. Fan, J. Guo and X. Peng, *Chem. Sci.*, 2019, 10, 10106-10112.

8 (a) M. Martinez-Alonso, N. Busto, D. L. Aguirre, L. Berlanga, M. C. Carrion, J. V. Cuevas, A. M. Rodriguez, A. Carbayo, B. R. Manzano, E. Ortí, F. A. Jalon, B. Garcia and G. Espino, *Chem. Eur. J.*, 2018, 24, 17523-17537. (b) J. Shen, T. W. Rees, Z. Zhou, S. Yang, L. Ji and H. Chao, *Biomaterials*, 2020, 251, 120079;

9 J. Zhao, S. Sun, X. Li W. Zhang and S. Gou , *ACS Appl. Bio. Mater*., 2019, 3, 252-262.

10 B. Liu, S. Monro, Z. Li, M. A. Jabed, D. Ramirez, C. G. Cameron K. Colón. J. Roque, S. Kilina, J. Tian, S. A. McFarland and W. Sun , *ACS Appl. Bio. Mater*., 2019, 2, 2964-2977.

11 Z. Feng, P. Tao , L. Zou, P. Gao, Y. Liu, X. Liu, H. Wang, S. Liu, Q. Dong, J. Liu, B. Xu, W. Huang and Q. Zhao, *ACS Appl. Mater.Interfaces*, 2017, 9, 28319-28330.

12 C. Wang, L. Lystrom, H. Yin, M. Hetu, S. Kilina, S. A. McFarland and W. Sun, *Dalton Trans*., 2016, 45, 16366-13678.

13 X. D. Bi, R. Yang, Y. C. Zhou, D.M. Chen, G. K. Li, Y. X. Guo, M. F. Wang, D.D. Liu and F. Gao, *Inorg. Chem.* 2020, 59, 14920–14931

14 E. M. Boreham, L. Jones, A. N. Swinburne, M. Blanchard-Desce, V. Hugues, C. Terryn, F. Miomandre, G. Lemercier and L. S. Natrajan, *Dalton Trans.*, 2015, 44, 16127

15 J. Zhao, S. C. Sun, X. Y. Li, W. J. Zhang and S. H. Gou, *ACS Appl. Bio Mater*. 2020, 3, 252−262

16 J. Zhao, X. Zhang, L. Fang, C. Gao, C. Xu and S. Gou, *Small*, 2020, 16, 2000363.

17 K. Qiu, M. Ouyan, Y. Liu, H. Huang, C. Liu, Y. Chen, L. Ji and H.Chao, *J. Mater. Chem. B*, 2017, 5, 5488-5498.

18 J. X. Zhang, M. Zheng, F. L. Zhang, B. Xu, W. J. Tian, Z. G. Xie, *Chem. Mater*. 2016, 28, 8825.

19 (a) Y. Cheng, J. Dai, C. L. Sun, R. Liu, T. Y. Zhai, X. D. Lou, F. Xia, *Angew. Chem., Int. Ed*. 2018, 57, 3123; (b) J. Qi, C. W. Sun, A. Zebibula, H. Q. Zhang, R. T. K. Kwok, X. Y. Zhao, W. Xi, J. W. Y. Lam, J. Qian, B. Z. Tang, *Adv. Mater*., 2018, 30, 1706856; (c) Y. H. Cheng, J. G. Wang, Z. J. Qiu, X. Y. Zheng, N. L. C. Leung, J. W. Y. Lam, B. Z. Tang, *Adv. Mater*., 2017, 29, 1703900.

20 J. H. Zhou, F. Qi, Y. C. Chen, S. R. Zhang, X. X. Zheng, W. J. He and Z. J. Guo, *Biosensors*, 2022, 12, 1027.

21 J. Li, J. Li, Y. Pu, S. Li, W. Gao and B. He, *Biomacromolecules*, 2021, 22, 1167-1176.

22 Y. Lu, G. Song, B. He, H. Zhang, X. Wang, D. Zhou, W. Dai and Q. Zhang, *Adv. Funct. Mater*., 2020, 30, 2004834.

23 J. Jin, Y. Zhu, Z. Zhang and W. Zhang, *Angew. Chem. Int. Ed.*, 2018, 57, 16354-16358.

24 D. Ma, C. Wu, K. Wu and C. Leung, *Molecules*, 2019, 24, 2739.

25 (a) Y. You, H. S. Huh, K. S. Kim, S. W. Lee, D. Kim and S. Y. Park, *Chem. Commun.*, 2008, 3998–4000; (b) S. Ladouceur and E. Zysman-Colman, *Eur. J. Inorg. Chem*., 2013, 2985-3007.

26 (a) L. Zhang, Y. Li, W. Che, D. Zhu, G. Li, Z. Xie, N. Song, S. Liu , B. Tang, X. Liu, Z. Su, and M. R. Bryce, *Adv. Sci*., 2019, 6, 802052; (b) L. Zhang, Y. Geng, L. Li, X. Tong, S. Liu, X. Liu, Z. Su, Z. Xie, D. Zhu and M. R. Bryce, *Chem. Sci*., 2021, 12, 5918–5925.

27 X. Li, D. Lee, J. Huang and J. Yoon, *Angew. Chem. Int. Ed*., 2018, 57, 9885-9890.

28 J. Zhao, X. Zhang, L. Fang, C. Gao, C. Xu and S. Gou, *Small*, 2020, 2000363.

29 Y. Zhang, H. Fu, S. Chen, B. Liu, W. Sun and H. Gao, *Chem. Commun*., 2020, 56, 762-765.

30 W. Zhang, W. Lin, Q. Pei, X. Hu, Z. Xie and X. Jing, *Chem. Mater*., 2016, 28, 4440-4446.

31 X. Li, B. Zheng, X.H. Peng,X. Li, J. Ying, Y. Zhao, J. Huang and J. Yoon, Coordin. *Chem. Rev*., 2019, 379, 147-160.

32 D. Chen, Q. Yu and X. Huang, *Small,* 2020, 16(23), 2001059.

33 (a) R. E. Daniels, L. K. McKenzie, J. R. Shewring, J. A. Weinstein, V. N. Kozhevnikov and H. E. Bryant, *RSC Adv*., 2018, 8, 9670-9676; (b) Y. Ma, S. Zhang, H. Wei, Y. Dong, L. Shen, S. Liu, Q. Zhao, L. Liu and W. Wong, *Dalton Trans*., 2018, 47, 5582-5588; (c) B. Hou, W. Zhang, C. Li, X. Sun, X. Feng and J. Liu, *Appl. Organomet. Chem*., 2022, 36, e6598.

34 C. Wang, P. Zhao, D. Jiang, G. Yang, Y. Xue, Z. Tang, M. Zhang, H. Wang, X. Jiang, Y. Wu, Y. Liu, W. Zhang and W. Bu, *ACS Appl. Mater. Interfaces*, 2020, 12, 5624–5632.

35 S. Ren, B. Wang, X. Zhu, D. Zhu, M. Liu, S. Li, Y. Yang, Z. Wang and H. Zhu, *ACS Appl. Mater. Interfaces*, 2020, 12, 24662–24674.

36 X. Yao, B. Yang, S. Wang, Z. Dai, D. Zhang, X. Zheng and Q. Liu, *J. Mater. Chem. B*, 2020, 8, 8010–8021.

37 Y. Liu, H. Wang, S. Li, C. Li, L. Xu, P. Huang, F. Liu, Y. Su, M. Qi, C. Yu and Y. Zhou, *Nat. Commun*., 2020, 11, 1724.

38 Q. Zou, M. Abbas, L. Zhao, S. Li, G. Shen and X. Yan, *J. Am. Chem. Soc*., 2017, 139, 1921-1927.

39 S. Liu, J. Han, Y. Chang, W. Wang, R. Wang, Z. Wang, G. Li, D. Zhu and M. Bryce, *Chem. Commun*., 2022, 58, 10056–10059

40 H. Wang , and G. Liu, *J. Mater. Chem. B*, 2018, 6, 4029-4042.

41 M. Chen, Y. Zheng, X. Cai, H. Zhang, F. Wang, C. Tan, W. Chen, L. Ji and Z. Mao, *Chem. Sci*., 2019, 10, 3315–3323.

42 J. Deng, H. Li, M. Yang and F. Wu, *Photochem. Photobiol. Sci*., 2020, 19, 905–912.

43 W. Lin, T. Sun, Z. Xie, J. Gu and X. Jing, *Chem. Sci*., 2016, 7, 1846-1852.

44 X. Zheng, L. Wang, Q. Pei, S. He, S. Liu and Z. Xie, *Chem. Mater*., 2017, 29, 2374–2381.

Electronic Supplementary Information (ESI)

Self-assembled nanoparticles based on cationic mono-/AIE tetra-nuclear Ir(III) complexes: long wavelength absorption/near-infrared emission photosensitizers for photodynamic therapy

Ziwei Wang,[a] Lijuan Li,[a] Weijin Wang,[a] Runlin Wang,[a] Guangzhe Li,[*c] Hang Bian,[*b] Dongxia Zhu[*a] and Martin R. Bryce[*d]

[a] *Key Laboratory of Nanobiosensing and Nanobioanalysis at Universities of Jilin Province, Department of Chemistry, Northeast Normal University, 5268 Renmin Street, Changchun, Jilin Province 130024, P. R. China.*

E-mail: zhudx047@nenu.edu.cn

[b] *Jilin Provincial Science and Technology Innovation Center of Health Food of Chinese Medicine, Changchun University of Chinese Medicine, Changchun, Jilin Province 130117, P. R. China.*

E-mail: 1993008106@qq.com

[c] *School of Material Science and Engineering, Jilin Jianzhu University, Changchun 130118, China.*

Email: bhspring@gmail.com

[d] *Department of Chemistry, Durham University, Durham, DH1 3LE, UK.*

E-mail: m.r.bryce@durham.ac.uk

†Electronic Supplementary Information (ESI) available: Supporting Figures and Tables. See DOI: 10.1039/x0xx00000x

‡The authors contributed equally to the preparation of this work.

Experimental Section

Materials and instruments

Materials for organic synthesis, poloxamer (F127) and indocyanine green (ICG) were purchased from Energy Chemical Company. RPMI Medium 1640 was purchased from Solarbio Life Science company. Fetal bovine serum (FBS) was purchased from Sigma-Aldrich. 3-(4,5-Dimethylthiazol-2-yl)-2,5-diphenyltetrazolium bromide (MTT) was obtained from Aladdin. 2',7'-Dichlorofluorescence diacetate (DCFH-DA) and the cell viability (live dead cell staining) assay kit were purchased from Shanghai Beyotime Biotechnology Co., Ltd.

^{1}H NMR spectra were recorded at 25 °C on a Varian 500 MHz spectrometer. UV-vis absorption spectra were recorded on a Shimadzu UV-3100 spectrophotometer. The photoluminescence spectra, excited state lifetimes (τ) and photoluminescence quantum yields (Φ_{PL}) were recorded on an Edinburgh FLS920 spectrofluorimeter under air at room temperature. Transmission electron microscopy (TEM) images of the samples were taken by a TECNAI F20 microscope. Diameter and diameter distribution of the nanoparticles were determined by a Malvern Zetasizer Nano instrument for dynamic light scattering (DLS). Confocal laser scanning microscopy (CLSM) images were taken using a ZeissLSM 700 (Zurich, Switzerland).

Synthesis of L1

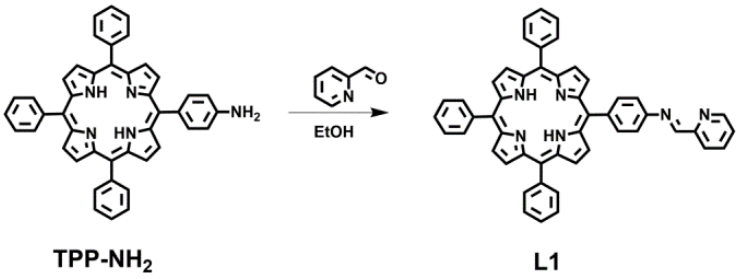

Scheme S1. Synthetic route to **L1**.

TPP-NH$_2$ (0.189 g, 0.3 mmol) and 2-pyridinecarboxaldehyde (0.039 g, 0.36 mmol) were added into ethanol (60 mL), and the mixture was stirred at 78 °C for 8 h. After

cooling to room temperature, the precipitate was filtered and recrystallized with ethanol to obtain the target compound with a yield of 83%. ^{1}H NMR (600 MHz, $CDCl_3$, δ [ppm]): 8.97 (s, 1H), 8.92 (d, J = 4.2 Hz, 2H), 8.88-8.81 (m, 7H), 8.40 (d, J = 7.7 Hz, 1H), 8.28 (d, J = 8.1 Hz, 2H), 8.24-8.20 (m, 6H), 7.94-7.91 (m, 1H), 7.80-7.74 (m, 9H), 7.70 (d, J = 7.8 Hz, 2H), 7.47-7.45 (m, 1H), -2.76 (s, 2H). Anal. Calcd. for $C_{50}H_{34}N_6$: C 83.54, H 4.77, N 11.69. Found C 83.49, H 4.52, N 11.65.

Synthesis of L4

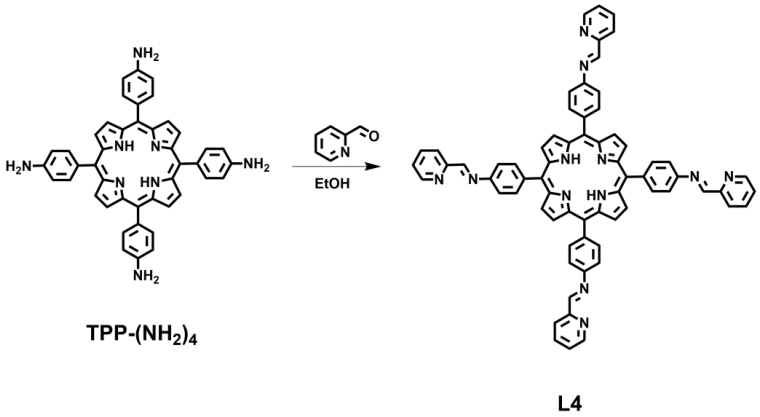

Scheme S2. Synthetic route to **L4**.

L4 was synthesized similarly to **L1**, except that **TPP-NH$_2$** was replaced by **TPP-(NH$_2$)$_4$** with a yield of 78%. ^{1}H NMR (600 MHz, $CDCl_3$, δ [ppm]): 8.98-8.91 (m, 6H), 8.82 (d, J = 4.2 Hz, 2H), 8.41 (d, J = 6.0 Hz, 2H), 8.31-8.27 (m, 4H), 7.94-7.91 (m, 2H), 7.73-7.69 (m, 4H), 7.47-7.45 (m, 2H), -2.69 (s, 1H). Anal. Calcd. for $C_{68}H_{46}N_{12}$: C 79.20, H 4.50, N 16.30. Found C 79.16, H 4.47, N 16.26.

Synthesis of [TPP-Ir]$^{+}$

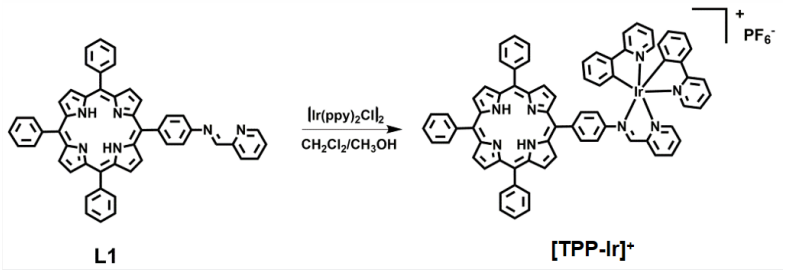

Scheme S3. Synthetic route to **[TPP-Ir]**$^{+}$.

$[Ir(ppy)_2Cl]_2$ (0.107 g, 0.1 mmol) and auxiliary ligand **L1** (0.144 g, 0.2 mmol) were dissolved in a mixture of methanol (30 mL) and dichloromethane (30 mL), and refluxed for 6 h under the protection of N_2. After cooling to room temperature, excess KPF_6 was added to the mixture (to replace counterion Cl^-). After stirring for 0.5 h, filtering to remove the excess potassium salts, and removal of the solvent from the filtrate by rotary evaporation, the crude product was obtained. Finally, the purple solid product was purified by column chromatography on silica gel (eluents dichloromethane /ethyl acetate 10/1, v/v) with a yield of 80%.^{1}H NMR (600 MHz, DMSO-d_6, δ [ppm]): 9.98 (s, 1H), 8.91-8.83 (m, 7H), 8.66 (d, J = 7.6 Hz, 1H), 8.55 (d, J = 4.4 Hz, 2H),8.41-8.37 (m, 2H), 8.32 (d, J = 8.4 Hz, 1H), 8.25-8.21 (m, 6H), 8.08-7.97 (m, 5H), 7.88-7.82 (m, 12H), 7.81-7.80 (m, 1H), 7.44-7.41 (m, 1H), 7.37-7.34 (m, 1H), 7.17 (d, J = 8.2 Hz, 2H), 7.10-7.06 (m, 1H), 7.04-7.01 (m, 1H), 6.97-6.94 (m, 1H), 6.92-6.88 (m, 1H), 6.34 (d, J = 7.3 Hz, 1H), 6.27 (d, J = 6.0 Hz, 1H), -2.97 (s, 2H). ^{13}C{^{1}H} NMR (151 MHz, DMSO-d_6, δ [ppm]) 170.45, 167.59, 167.10, 156.02, 151.60, 150.80, 150.67, 149.97, 149.66, 147.54, 144.44, 144.33, 141.63, 141.14, 140.39, 139.58, 139.39, 134.66, 134.27, 131.79, 131.04, 130.71, 130.35, 128.64, 127.54, 127.49, 125.65, 125.20, 124.73, 124.47, 122.98, 122.70, 121.10, 120.78, 120.64, 120.12, 118.89. MS: [m/z] = 1219.3624 (calcd $C_{72}H_{50}IrN_8$ for M^+: 1219.38). Anal. Calcd. for $C_{72}H_{50}F_6IrN_8P$: C 63.38, H 3.69, N 8.21. Found C 63.42, H 3.75, N 8.18.

Synthesis of [TPP-4Ir]$^{4+}$

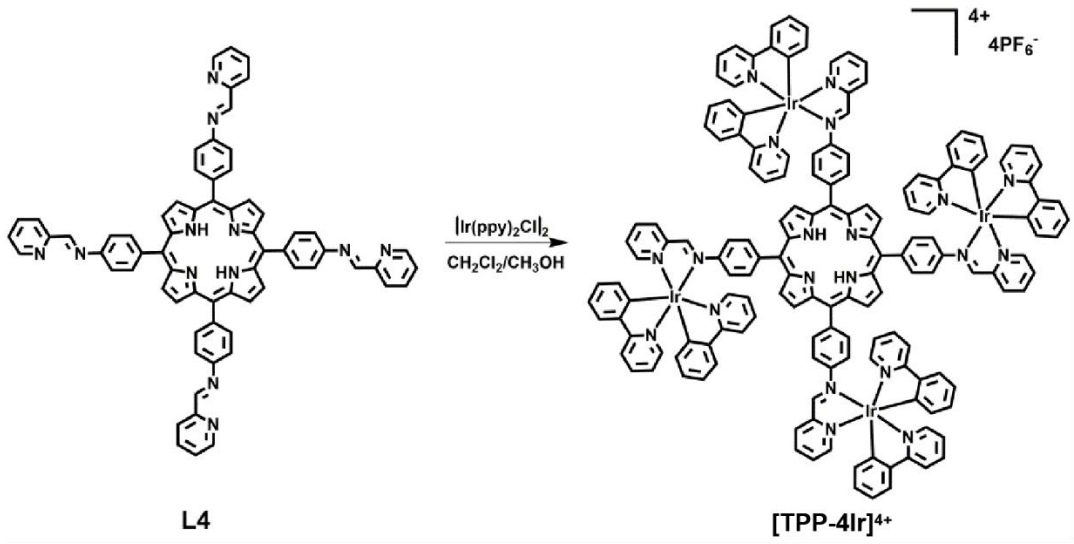

Scheme S4. Synthetic route of **[TPP-4Ir]$^{4+}$**.

The synthesis and purification of **[TPP-4Ir]$^{4+}$** was similar to that of **[TPP-Ir]$^{+}$**, $[Ir(ppy)_2Cl]_2$ (0.214 g, 0.2 mmol) and auxiliary ligand **L4** (0.1030 g, 0.1 mmol) were dissolved in a mixture of methanol (30 mL) and dichloromethane (30 mL), and refluxed for 8 h under the protection of N_2. After cooling to room temperature, excess KPF_6 was added to the mixture (to replace counterion Cl^-). After stirring for 0.5 h, filtering to remove the excess potassium salts, and removal of the solvent from the filtrate by rotary evaporation, the product was obtained without other purified process. The product is pure and the product yield is 99%. ^{1}H NMR (600 MHz, DMSO-d_6, δ [ppm]): 10.03-9.90 (m, 1H), 8.87-8.81 (m, 1H), 8.72-8.66 (m, 1H), 8.58 (s, 1H), 8.42-8.38 (m, 2H), 8.31-8.27 (m, 1H), 8.08-7.82 (m, 10H), 7.48-7.43 (m, 1H), 7.40-7.36 (m, 1H), 7.29-7.19 (m, 2H), 7.11-7.00 (m, 2H), 6.99-6.91 (m, 2H), 6.37-6.25 (m, 2H), -3.15 (s, 0.5H). ^{13}C{^{1}H} NMR (151 MHz, DMSO-d_6, δ [ppm]) 170.67, 170.64, 167.54, 167.49, 167.13, 155.97, 151.46, 151.10, 151.07, 150.72, 150.12, 150.09, 149.52, 147.86, 144.50, 144.33, 140.90, 140.45, 139.61, 139.48, 134.37, 132.01, 131.92, 131.64, 131.13, 130.78, 130.35, 125.68, 124.99, 124.74, 124.64, 123.05, 122.51, 121.15, 121.14, 120.81, 120.76, 120.14, 119.42. MS: (M^{4+}) [m/z] = 758.5155 (calcd for $C_{156}H_{110}Ir_4N_{20}$: 3034.77). Anal. Calcd. for $C_{156}H_{110}F_{24}Ir_4N_{20}P_4$: C 51.85, H 3.07, N 7.75. Found C 51.79, H 3.11, N 7.81.

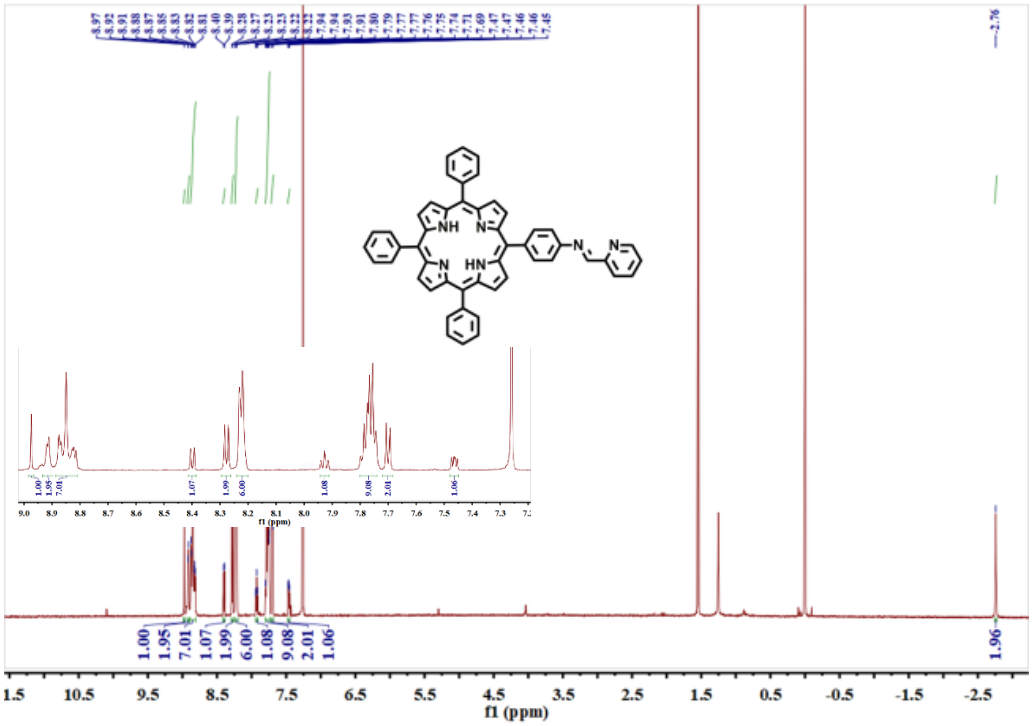

Fig. S1 ^{1}H NMR spectrum of **L1** in $CDCl_3$.

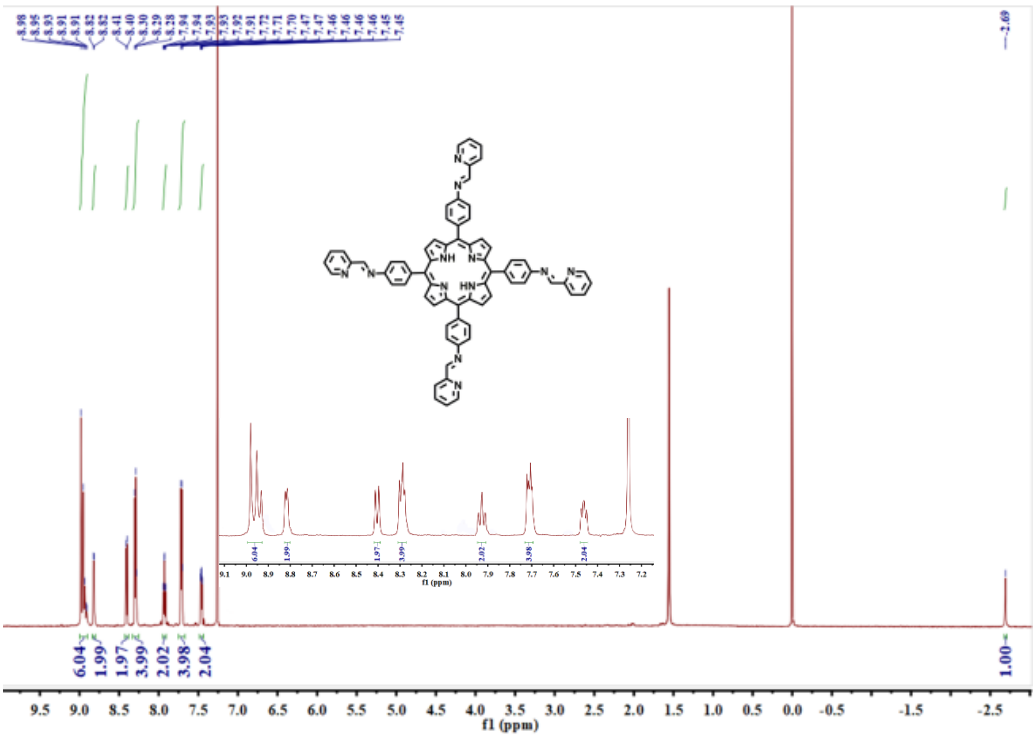

Fig. S2 ^{1}H NMR spectrum of **L4** in $CDCl_3$.

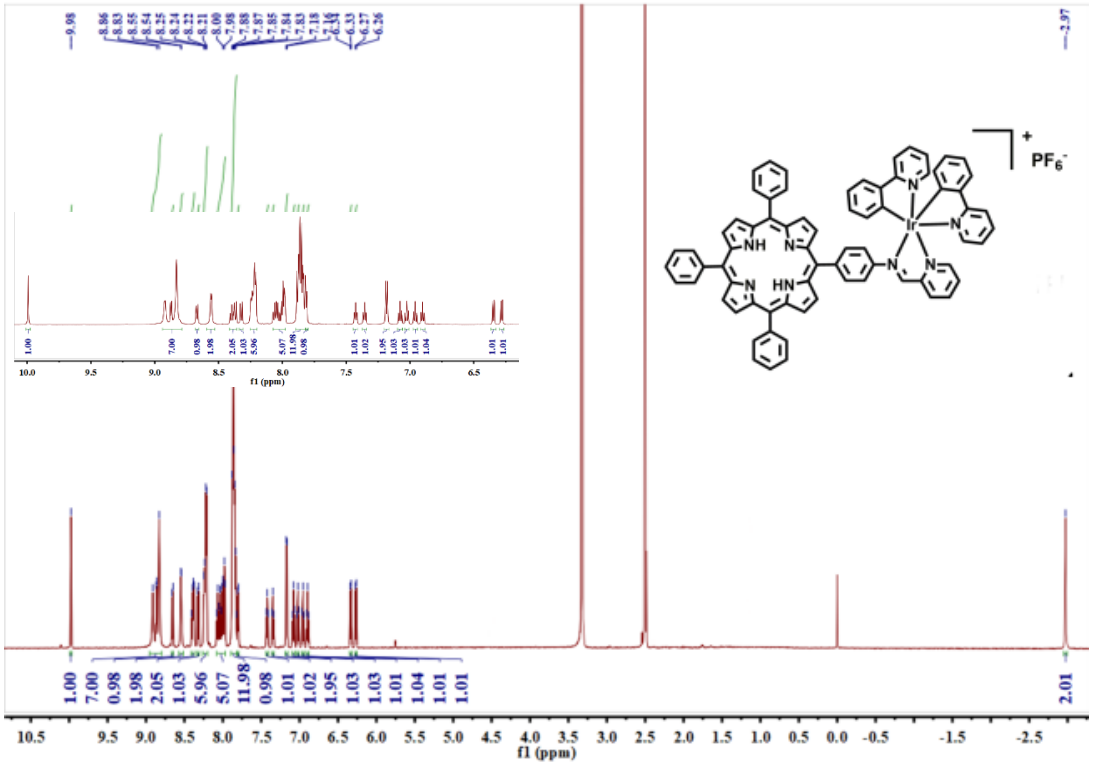

Fig. S3 ^{1}H NMR spectrum of **[TPP-Ir]**$^{+}$ in DMSO-d_6.

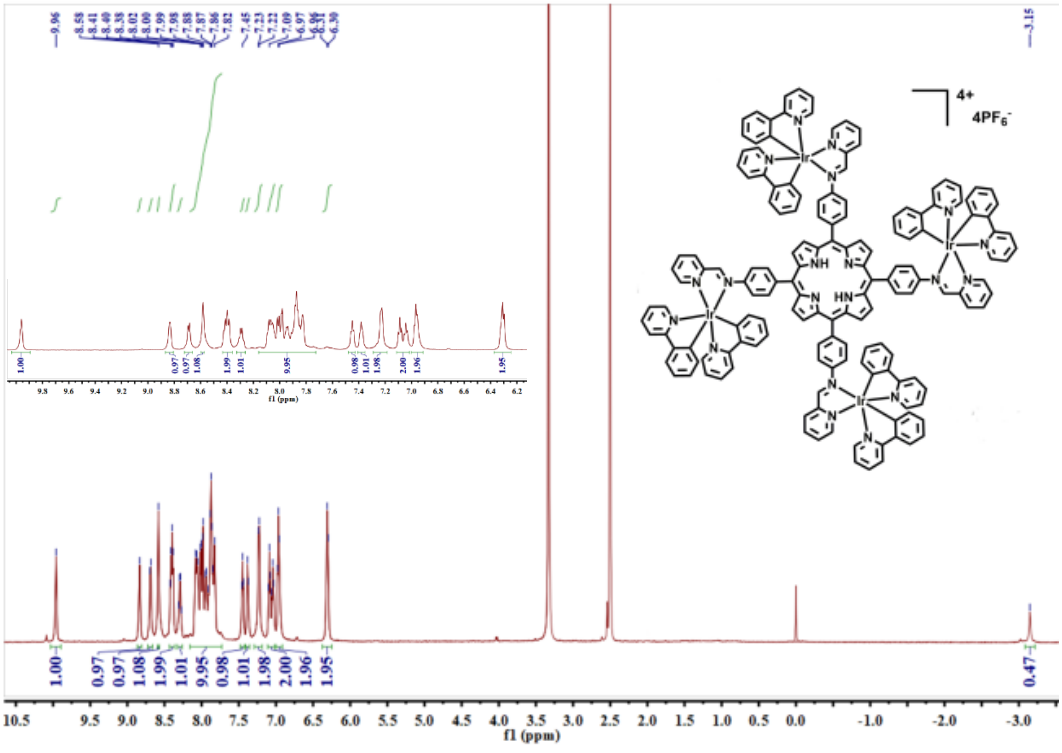

Fig. S4 ^{1}H NMR spectrum of **[TPP-4Ir]**$^{4+}$ in DMSO-d_6.

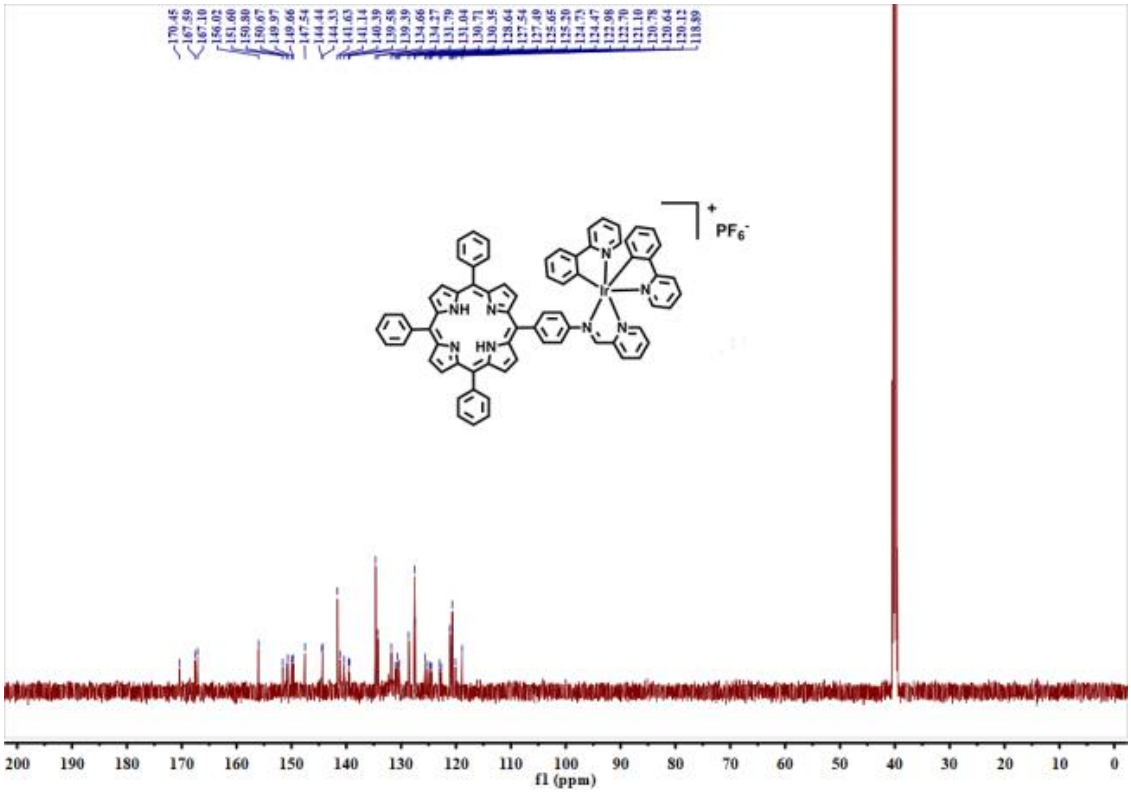

Fig. S5 ^{13}C NMR spectrum of **[TPP-Ir]**$^{+}$ in DMSO-d_6.

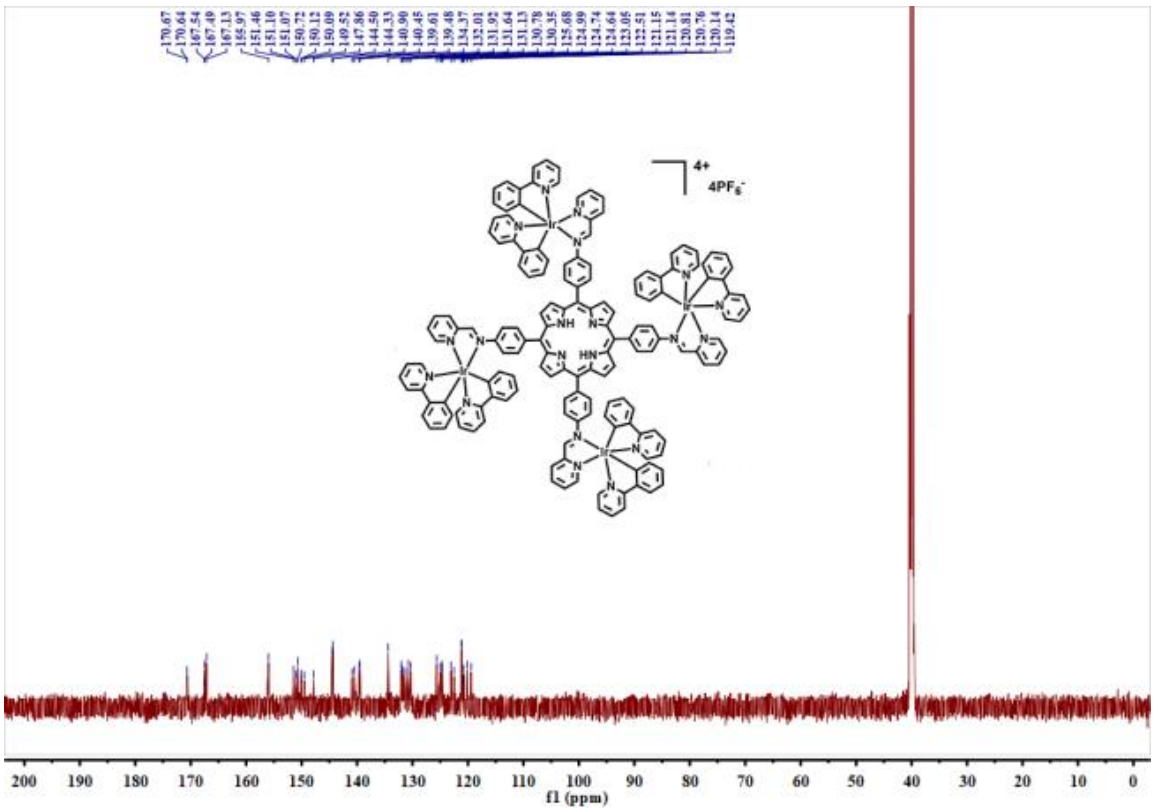

Fig.S6 ^{13}C NMR spectrum of **[TPP-4Ir]**$^{4+}$ in DMSO-d_6.

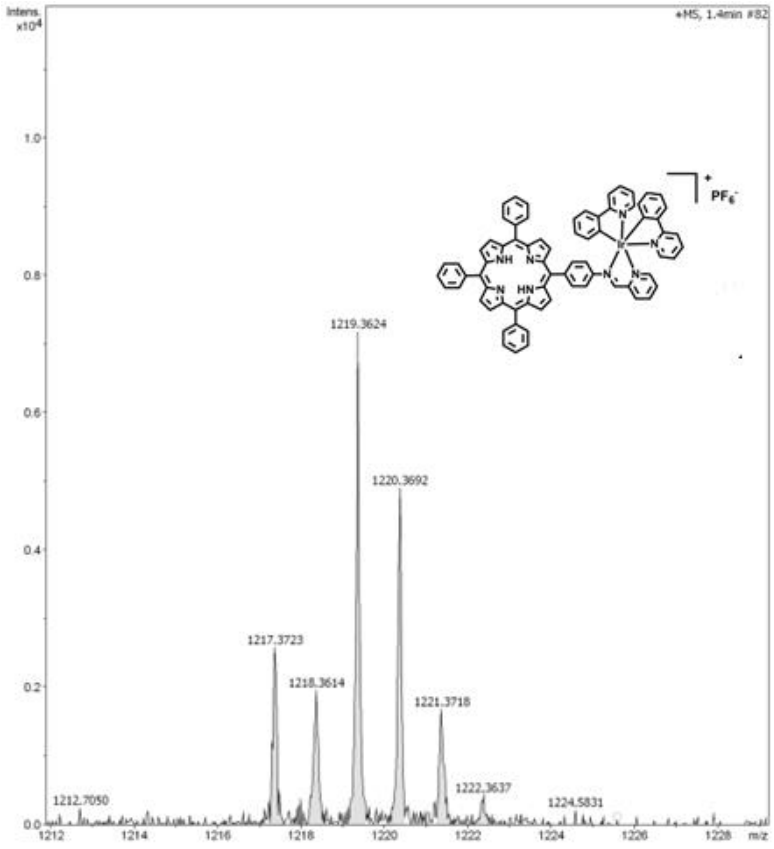

Fig. S7 ESI mass spectrum of **[TPP-Ir]**$^{+}$.

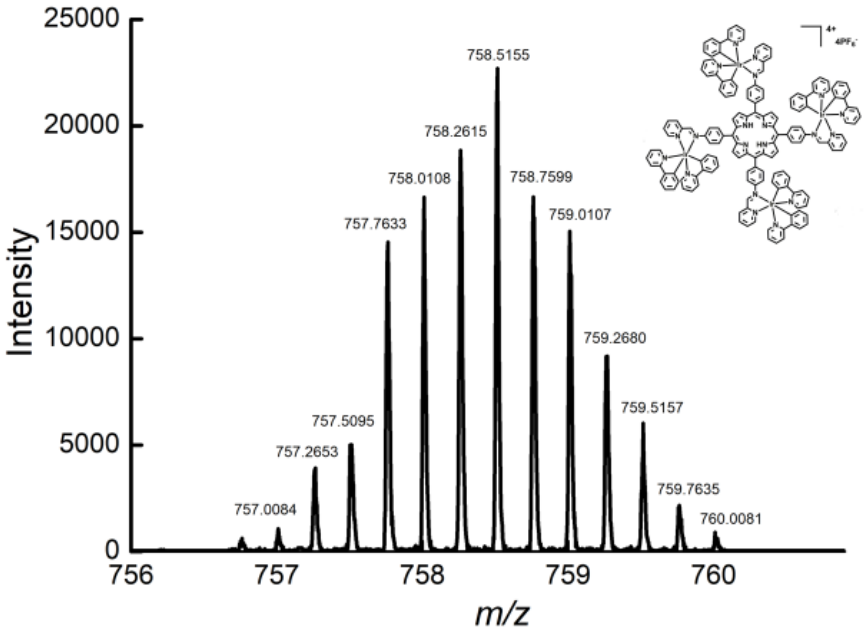

Fig. S8 ESI mass spectrum of **[TPP-4Ir]**$^{4+}$.

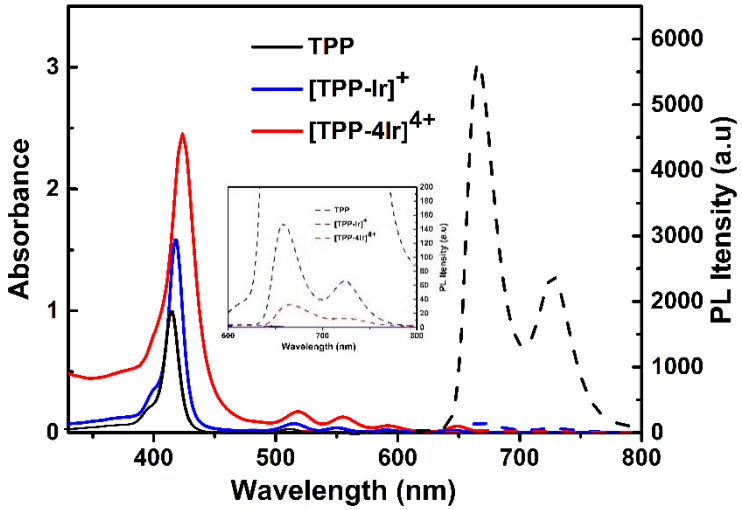

Fig. S9 The UV–vis absorption spectra in CH_3COCH_3 (solid line) and the PL spectra in CH_3COCH_3 of **[TPP]**, **[TPP-Ir]**$^{+}$ and **[TPP-4Ir]**$^{4+}$ (10^{-5} M) (dashed line). Inset is an expansion of PL spectra in the 600-800 nm region.

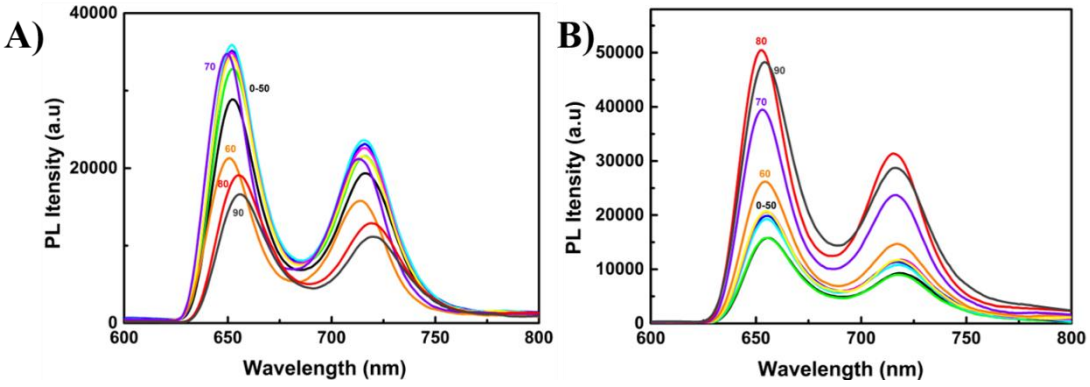

Fig. S10 PL spectra of **[TPP-Ir]** $^{+}$ (A) and **[TPP-4Ir]**$^{4+}$ (B) in acetone-H_2O mixtures (complex concentration = 1.0 $\times 10^{-5}$ M) with different water fractions (0-90% v/v) at room temperature.

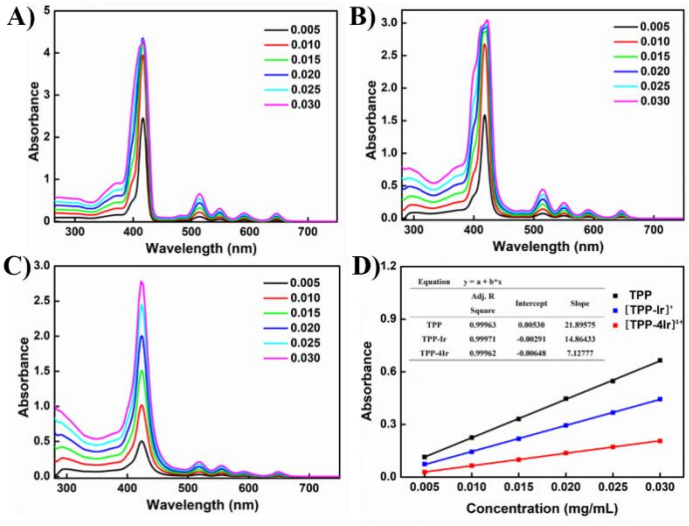

Fig. S11 UV-vis absorption spectra of A) **TPP** NPs, B) **[TPP-Ir]**$^{+}$ NPs and C) **[TPP-4Ir]**$^{4+}$ NPs in DMF/H_2O = 4/1 (v/v) concentration; D) Standard curves of **TPP** NPs, **[TPP-Ir]**$^{+}$ NPs and **[TPP-4Ir]**$^{4+}$ NPs in DMF/H_2O = 4/1 (v/v).

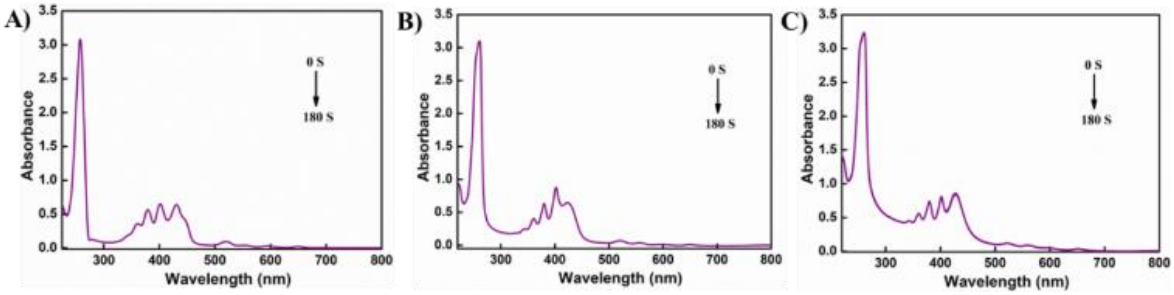

Fig. S12 UV-visible absorption spectra of ABDA in the presence of A) **TPP** NPs, B) **[TPP-Ir]**$^{+}$ NPs and C) **[TPP-4Ir]**$^{4+}$ NPs (5×10^{-6} M) without light.

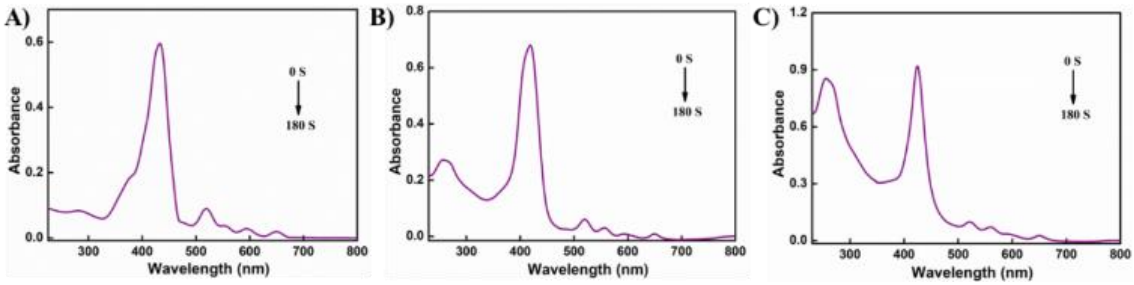

Fig. S13 UV-visible absorption spectra of A) **TPP** NPs, B) **[TPP-Ir]**$^{+}$ NPs

and C) **[TPP-4Ir]**$^{4+}$ NPs (5×10^{-6} M) upon irradiation of a white LED at 20 mW cm^{-2}.

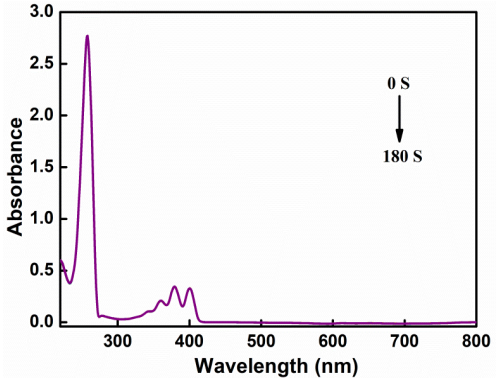

Fig. S14 UV-visible absorption spectra of ABDA upon irradiation of a white LED at 20 mW cm^{-2}.

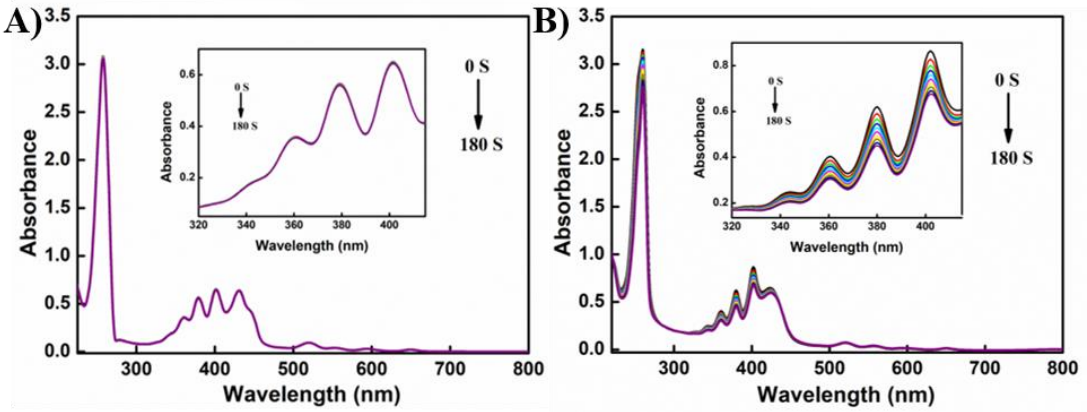

Fig. S15 UV-visible absorption spectra of ABDA in the presence of A) **[TPP-Ir]**$^{+}$ NPs and B) **[TPP-4Ir]**$^{4+}$ NPs (5×10^{-6} M) upon irradiation with a white LED at 20 mW cm^{-2}.

Table S1 Photophysical data of **TPP** NPs, **[TPP-Ir]**$^{+}$ NPs and **[TPP-4Ir]**$^{4+}$ NPs

	λ_{abs} (nm)	λ_{em} (nm)	Φ_P (%)	τ_P (ns)	k_r^b ($\times 10^6$ s^{-1})	k_{nr}^b ($\times 10^8$ s^{-1})
TPP NPs[a]	251; 429; 519; 555; 594; 649	656; 717	27.1	5.47	49.45	1.33
[TPP-Ir]$^{+}$ NPs[a]	257; 417; 520; 558; 594; 650	656; 720	8.1	5.72	14.21	1.61
[TPP-4Ir]$^{4+}$ NPs[a]	256; 424; 521; 560; 594; 650	656; 720	3.6	5.87	6.12	1.64

[a] Measured in water, λ_{ex} = 365 nm, concentration is 1.0×10^{-5} M. Radiative transition value k_r and non-radiative transition value k_{nr} are calculated according to the following formula, which is: k_r =

Φ/τ and k_{nr} = (1-Φ)/τ, Φ is the fluorescence quantum efficiency, τ is the phosphorescence lifetime value.

Table S2 Molar absorption coefficient (ε) of **TPP** NPs, **[TPP-Ir]**$^{+}$ NPs and **[TPP-4Ir]**$^{4+}$ NPs

	$\lambda^{[b]}_{max}$ **(nm)**	$\varepsilon^{[b]}$ **(M^{-1} cm^{-1})**
TPP NPs[a]	251; 429; 519; 555; 594; 649	10020; 115730; 9460; 3893; 3034; 2175
[TPP-Ir]$^{+}$ NPs[a]	257; 417; 520; 558; 594; 650	54090; 138510; 13770; 7994; 4918; 4018
[TPP-4Ir]$^{4+}$ NPs[a]	256; 424; 521; 560; 594; 650	163510; 184870; 20060; 15420; 9379; 6858

[a] Measured in water, concentration is 1.0×10^{-5} M.

[b] The maximum absorption wavelength and corresponding molar absorption coefficient of **TPP** NPs, **[TPP-Ir]**$^{+}$ NPs and **[TPP-4Ir]**$^{4+}$ NPs.